An Efficient and Unconditionally Stable UPML for Structure-Preserving Multisymplectic FDTD Domains

Zhipeng Chen, Linqing Li, Wei E. I. Sha, *Senior Member, IEEE*, Zhixiang Huang, *Senior Member, IEEE*, Xianliang Wu, and Kaikun Niu, *Member, IEEE*

***Abstract*—This article proposes a structure-preserving implementation of the uniaxial perfectly matched layer (UPML) within the multisymplectic finite-difference time-domain (MS-FDTD) framework. Based on the Preissmann scheme, the proposed method introduces anisotropic damping terms without breaking the geometric structure of Maxwell's equations. By employing a local 1-D (LOD) splitting strategy, the UPML is naturally embedded into the MS-FDTD method, avoiding corner or edge-specific treatments and simplifying implementation, all while preserving the original multisymplectic (MS) properties. A spectral stability analysis confirms that the method is unconditionally stable in three dimensions. Numerical experiments involving a perfectly electrically conducting (PEC) plate, multilayer dielectric slabs, and power distribution network and human brain tissues demonstrate the method's outstanding absorption performance and accuracy, even under large Courant-Friedrichs-Lewy (CFL) conditions. Compared to the conventional finite-difference time-domain (FDTD) method and commercial solvers, the proposed method shows clear advantages in structural preservation and stability, while each approach maintains its own strengths in terms of computational cost and modeling flexibility. Overall, the proposed method enhances the practical applicability of the MS-FDTD method for open-region electromagnetic problems, offering a robust and efficient solution for large-scale time-domain simulations.**

***Index Terms*—Finite-difference time-domain (FDTD), local 1-D (LOD), multisymplectic (MS), stability analysis, uniaxial perfectly matched layer (UPML).**

I. INTRODUCTION

ACCURATELY and stably simulating electromagnetic wave propagation in complex media and bounded domains remains one of the core challenges in computational electrodynamics. In recent years, the structure-preserving geometric algorithms [1]—especially symplectic [2], [3], [4], [5] and multisymplectic (MS) [6], [7] integrators—have received increasing attention due to their long-term stability and local conservation properties in time-domain simulations. In particular, the MS schemes constructed for Maxwell's equations [8], [9], [10], [11], [12] (collectively referred to as the MS Maxwell solvers) have demonstrated remarkable performance in both theoretical analysis and engineering applications [13], [14].

Unlike conventional numerical methods that primarily focus on global conservation of quantities, such as energy or momentum, MS methods preserve the structural properties of the system in both time and space by satisfying local MS conservation laws (MSCLs) [15]. This structural preservation enables better maintenance of the physical consistency of wave systems over long simulations. When applied to hyperbolic partial differential equations, such as Maxwell's equations, these methods offer superior numerical dispersion characteristics, enhanced stability, and improved physical fidelity. It is worth noting that in source-free, isotropic, and homogeneous media, Maxwell's equations inherently possess an MS structure, which provides a strong theoretical foundation for the application of such schemes. In practical finite-difference time-domain (FDTD) simulations [16], [17], external sources must be included to excite electromagnetic fields. The presence of these sources formally breaks the exact MSCL, but this does not undermine the framework. The MS discretization still preserves the geometric structure of the homogeneous system, while the sources act as external forcing terms. This situation is analogous to the forced Hamiltonian systems, where the symplectic structure of the unforced part remains meaningful and beneficial for stability and accuracy.

Based on this framework, we pioneered the engineering application of the structure-preserving MS theory from the field of mathematics to electromagnetics, proposing an MS algorithm for electromagnetic computation, termed as a 3-D MS-FDTD method [18]. This method discretizes Maxwell's equations using the Preissmann MS scheme and applies a locally 1-D (LOD) [19], [20], [21], [22], [23], [24], [25] decomposition strategy for dimensional splitting. The resulting method significantly reduces the computational cost associated

Received 12 August 2025; revised 10 October 2025 and 10 November 2025; accepted 12 November 2025. Date of publication 24 November 2025; date of current version 6 February 2026. This work was supported in part by the National Natural Science Foundation of China under Grant 62471002, Grant U22A2017, and Grant 62531001; in part by Anhui Province Science and Technology Innovation Tackle Plan Project under Grant 202423k09020033; and in part by the State Key Laboratory of Radio Frequency Heterogeneous Integration (Open Scientific Research Program) under Grant KF2024001. *(Corresponding author: Kaikun Niu.)*

Zhipeng Chen, Linqing Li, Zhixiang Huang, Xianliang Wu, and Kaikun Niu are with the State Key Laboratory of Opto-Electronic Information Acquisition and Protection Technology, Anhui University, Hefei 230601, China (e-mail: kkniu@ahu.edu.cn).

Wei E. I. Sha is with the Key Laboratory of Advanced Micro/Nano Electronic Devices and Smart Systems of Zhejiang Province, Innovative Institute of Electromagnetic Information and Electronic Integration, College of Information Science and Electronic Engineering, Zhejiang University, Hangzhou 310058, China.

Digital Object Identifier 10.1109/TMTT.2025.3633271

with solving high-dimensional implicit systems while maintaining the discrete MS structure, leading to unconditional stability and high accuracy.

However, extending the structure-preserving algorithms like MS-FDTD to practical electromagnetic simulations [26] in open domains presents a major challenge: the efficient and stable implementation of absorbing boundary conditions [27]. In conventional FDTD frameworks, perfectly matched layers (PMLs) [28], [29], [30], [31], [32] are widely used to simulate open boundaries, especially improved versions, such as convolutional PML (CPML) [33], [34], [35] and uniaxial PML (UPML) [36], which are known for their excellent absorption performance. Nonetheless, directly introducing these PML formulations into an MS framework is nontrivial, as the artificial anisotropic lossy media introduced by PMLs can potentially break the geometric structure of the original system, particularly the discrete MS conservation properties.

To address this issue, in this article, we propose the unconditionally stable UPML algorithm, which is fully compatible with the MS-FDTD method while preserving its structure-preserving properties. Meanwhile, it can effectively truncate the simulation space with remarkable accuracy and efficiency. The main contributions of this work are summarized as follows.

1) We propose a UPML absorbing boundary scheme tailored for the MS MS-FDTD method, in which the MS structure is rigorously extended into the anisotropic lossy media of the PML region. This ensures that the structural consistency, physical fidelity, and unconditional stability of the MS-FDTD scheme are fully preserved while achieving highly efficient absorption.

2) To achieve an efficient and practical implementation, the proposed MS UPML scheme is embedded into the LOD-decomposed MS-FDTD framework. This decomposition transforms the multidimensional update into a sequence of 1-D substeps, allowing the anisotropic damping tensors of UPML to be incorporated without altering the MS structure or its unconditional stability. At the same time, it numerically decomposes the fully coupled multidimensional update into directional substeps, thereby reducing computational complexity while ensuring that the underlying physical multidimensional coupling is naturally preserved through the accumulated operator action.

3) Unlike traditional FDTD implementations, which require complex corner and edge treatments when using PMLs, the proposed UPML implementation under the LOD scheme eliminates the need for such special handling. This contributes to the structural simplicity and implementation robustness of the method, making it highly compatible with the MS-FDTD framework.

4) The stability and absorption performance of the proposed MS-FDTD-UPML method have been systematically evaluated under various simulation conditions. The results demonstrate consistently low-reflection errors below −60 dB, indicating excellent absorption efficiency and unconditional stability. Notably, thanks to the intrinsic structure-preserving property of the MS scheme, the absorption performance of the UPML does not deteriorate even under large time-step settings. This highlights the unique advantage of the MS formulation in modeling strongly coupled absorbing boundaries.

5) To further validate the proposed method, several challenging and representative scenarios were investigated, including multilayer dielectric structures with strong interference effects, on-chip field distributions in a power distribution network, and highly inhomogeneous human brain models. The simulation results confirm that the structure-preserving MS-FDTD method achieves both high computational efficiency and accuracy in these realistic applications, demonstrating its suitability for large-scale and high-fidelity electromagnetic wave modeling.

The remainder of this article is organized as follows. Section II reviews the MS formulation of Maxwell's equations and introduces the proposed structure-consistent extension for UPML. Section III analyzes the stability of the UPML model within the MS-FDTD framework and examines the directional subsystem stability under LOD splitting. Section IV presents several numerical examples and comparisons with conventional FDTD methods. Finally, Section V concludes this article and discusses potential directions for future research.

II. FORMULATION

The set of the MS Maxwell's equations in each isotropic, homogeneous, nondissipative medium is

$$\mathbf{M}\left(\frac{\partial \boldsymbol{\psi}}{\partial t}\right)+\mathbf{K_1}\left(\frac{\partial \boldsymbol{\psi}}{\partial x}\right)+\mathbf{K_2}\left(\frac{\partial \boldsymbol{\psi}}{\partial y}\right)+\mathbf{K_3}\left(\frac{\partial \boldsymbol{\psi}}{\partial z}\right)=\nabla \mathrm{S}\left(\boldsymbol{\psi}\right) \tag{1}$$

where

$$\mathrm{S}\left(\psi\right)=\frac{1}{2}\left(\varepsilon\left|\boldsymbol{E}\right|^{2}+\mu\left|\boldsymbol{H}\right|^{2}\right)$$

$$\varepsilon=\varepsilon_0\varepsilon_r\ \mu=\mu_0\mu_r$$

$$\mathbf{M}=\begin{bmatrix}0 & -\boldsymbol{I}_{3\times 3}\\ \boldsymbol{I}_{3\times 3} & 0\end{bmatrix}\mathbf{K_1}=\begin{bmatrix}\begin{matrix}0 & 0 & 0\\ 0 & 0 & -\frac{1}{\varepsilon}\\ 0 & \frac{1}{\varepsilon} & 0\end{matrix} & \boldsymbol{O}_{3\times 3}\\ \boldsymbol{O}_{3\times 3} & \begin{matrix}0 & 0 & 0\\ 0 & 0 & -\frac{1}{\mu}\\ 0 & \frac{1}{\mu} & 0\end{matrix}\end{bmatrix}$$

$$\mathbf{K}_2=\begin{bmatrix}\begin{matrix}0 & 0 & \frac{1}{\varepsilon}\\ 0 & 0 & 0\\ -\frac{1}{\varepsilon} & 0 & 0\end{matrix} & \boldsymbol{O}_{3\times 3}\\ \boldsymbol{O}_{3\times 3} & \begin{matrix}0 & 0 & \frac{1}{\mu}\\ 0 & 0 & 0\\ -\frac{1}{\mu} & 0 & 0\end{matrix}\end{bmatrix}$$

$$\mathbf{K}_3=\begin{bmatrix}\begin{matrix}0 & -\frac{1}{\varepsilon} & 0\\ \frac{1}{\varepsilon} & 0 & 0\\ 0 & 0 & 0\end{matrix} & \boldsymbol{O}_{3\times 3}\\ \boldsymbol{O}_{3\times 3} & \begin{matrix}0 & -\frac{1}{\mu} & 0\\ \frac{1}{\mu} & 0 & 0\\ 0 & 0 & 0\end{matrix}\end{bmatrix}.$$

Here, $\boldsymbol{\psi}=(E_x,\ E_y,\ E_z,\ H_x,\ H_y,\ H_z)^{\mathrm{T}}$ is the state vector consisting of the electric and magnetic field components, **M**,

K1, **K2,** and **K3** are all symplectic matrices, and $S(\psi)$ denotes the energy density function. Next, the anisotropic medium PML method is introduced to modify the MS Maxwell's equations

$$\mathbf{M}\left(\frac{\partial\psi}{\partial t}\right)+\mathbf{K_1}\left(\frac{\partial\psi}{s_x\partial x}\right)+\mathbf{K_2}\left(\frac{\partial\psi}{s_y\partial y}\right)+\mathbf{K_3}\left(\frac{\partial\psi}{s_z\partial z}\right) = \nabla \mathrm{S}(\psi)_{\mathrm{upml}} \tag{2}$$

where

$$\mathrm{S}(\psi)_{\mathrm{upml}} = \frac{1}{2}\left(\varepsilon \boldsymbol{S}_E\,|\boldsymbol{E}|^2+\mu \boldsymbol{S}_H\,|\boldsymbol{H}|^2\right)$$

$$S_E = \begin{bmatrix} s_y s_z & 0 & 0\\ 0 & s_x s_z & 0\\ 0 & 0 & s_y s_x\end{bmatrix} S_H = \begin{bmatrix} s_y s_z & 0 & 0\\ 0 & s_x s_z & 0\\ 0 & 0 & s_y s_x\end{bmatrix}^{-1}$$

$$s_\eta = \kappa_\eta + \frac{\sigma_\eta}{j\omega\varepsilon_0}, \quad \eta = x, y, z$$

where $S(\psi)_{\mathrm{upml}}$ characterizes the absorption effect of the UPML layer on the electromagnetic field, leading to a gradual decay of the system energy. $S_{\mathbf{E}}$ and $S_{\mathbf{H}}$ represent the electric and magnetic energy forms, respectively, corresponding to the matrix representations of the electric and magnetic energy densities. In the absence of PML, $S_{\mathbf{E}}$ reduces to the same form as that used in the conventional FDTD scheme. In this context, we explicitly present the updated equations for the UPML-extended MS formulation in the *Ex* and *Hx* directions, which correspond to the *x*-directed components of the electromagnetic field. The full set of equations, including those for the *y* and *z* components, can be systematically obtained by cyclically permuting the coordinate indexes $x \to y \to z$. This ensures that the structure-preserving UPML formulation remains fully defined and symmetric across all spatial directions. The following equations illustrate the specific formulation for the *x*-directed components under this framework:

$$\frac{\partial H_z}{\partial y}-\frac{\partial H_y}{\partial z} = \kappa_y\frac{\partial D_x}{\partial t}+\frac{\delta_y}{\varepsilon_0}D_x \tag{3}$$

$$\kappa_x\frac{\partial D_x}{\partial t}+\frac{\delta_x}{\varepsilon_0}D_x = \varepsilon_1\kappa_z\frac{\partial E_x}{\partial t}+\frac{\varepsilon_1}{\varepsilon_0}\delta_z E_x \tag{4}$$

$$\frac{\partial E_z}{\partial y}-\frac{\partial E_y}{\partial z} = -\kappa_y\frac{\partial B_x}{\partial t}-\frac{\delta_y}{\varepsilon_0}B_x \tag{5}$$

$$\kappa_x\frac{\partial B_x}{\partial t}+\frac{\delta_x}{\varepsilon_0}B_x = \mu_1\kappa_z\frac{\partial H_x}{\partial t}+\frac{\mu_1}{\varepsilon_0}\delta_z H_x \tag{6}$$

where

$$\varepsilon_1 = \varepsilon_0\varepsilon_{r1}$$

$$\mu_1 = \mu_0\mu_{r1}$$

$$\begin{bmatrix} D_x\\ D_y\\ D_z\end{bmatrix} = \varepsilon_1\begin{bmatrix}\frac{s_y s_z}{s_x} & & \\ & \frac{s_x s_z}{s_y} & \\ & & \frac{s_x s_y}{s_z}\end{bmatrix}\begin{bmatrix} E_x\\ E_y\\ E_z\end{bmatrix}$$

$$\begin{bmatrix} B_x\\ B_y\\ B_z\end{bmatrix} = \mu_1\begin{bmatrix}\frac{s_y s_z}{s_x} & & \\ & \frac{s_x s_z}{s_y} & \\ & & \frac{s_x s_y}{s_z}\end{bmatrix}\begin{bmatrix} H_x\\ H_y\\ H_z\end{bmatrix}.$$

Here, D and B are the intermediate variables, and ε_1 and μ_1 denote the permittivity and permeability within the absorbing region, respectively. ε_r and μ_r represent the relative permittivity and permeability, and ε_0 and μ_0 correspond to those in free space. By substituting the Preissmann discretization operator [18] (i.e., the implicit midpoint scheme) into (3)–(6) and performing straightforward algebraic manipulations, one can obtain the discrete form of the MS Maxwell system incorporating the UPML absorbing boundary. This formulation preserves the geometric structure of the original equations, as shown in the following equations:

$$\begin{cases}\left(D^{n+1}_{x_{i,j+1,k+1}}+D^{n+1}_{x_{i,j,k+1}}+D^{n+1}_{x_{i,j+1,k}}+D^{n+1}_{x_{i,j,k}}\right)\\ -CB_x\left(H^{n+1}_{z_{i,j+1,k+1}}+H^{n+1}_{z_{i,j+1,k}}-H^{n+1}_{z_{i,j,k+1}}-H^{n+1}_{z_{i,j,k}}\right)\\ +CB_x\left(H^{n+1}_{y_{i,j+1,k+1}}+H^{n+1}_{y_{i,j+1,k}}-H^{n+1}_{y_{i,j,k+1}}-H^{n+1}_{y_{i,j,k}}\right)\\ =CA_x\cdot\left(D^{n}_{x_{i,j+1,k+1}}+D^{n}_{x_{i,j,k+1}}+D^{n}_{x_{i,j+1,k}}+D^{n}_{x_{i,j,k}}\right)\\ +CB_x\left(H^{n}_{z_{i,j+1,k}}+H^{n}_{z_{i,j+1,k}}-H^{n}_{z_{i,j,k+1}}-H^{n}_{z_{i,j,k}}\right)\\ -CB_x\left(H^{n}_{y_{i,j+1,k+1}}+H^{n}_{y_{i,j+1,k}}-H^{n}_{y_{i,j,k+1}}-H^{n}_{y_{i,j,k}}\right)\end{cases} \tag{7}$$

$$E^{n+1}_{x_{i,j,k}}-C2_x\cdot D^{n+1}_{x_{i,j,k}} = C1_x\cdot E^{n}_{x_{i,j,k}}-C3_x\cdot D^{n}_{x_{i,j,k}} \tag{8}$$

$$\begin{cases}\left(B^{n+1}_{x_{i,j+1,k+1}}+B^{n+1}_{x_{i,j,k+1}}+B^{n+1}_{x_{i,j+1,k}}+B^{n+1}_{x_{i,j,k}}\right)\\ +CQ_x\left(E^{n+1}_{z_{i,j+1,k+1}}+E^{n+1}_{z_{i,j+1,k}}-E^{n+1}_{z_{i,j,k+1}}-E^{n+1}_{z_{i,j,k}}\right)\\ -CQ_x\left(E^{n+1}_{y_{i,j+1,k+1}}+E^{n+1}_{y_{i,j+1,k}}-E^{n+1}_{y_{i,j,k+1}}-E^{n+1}_{y_{i,j,k}}\right)\\ =CP_x\cdot\left(B^{n}_{x_{i,j+1,k+1}}+B^{n}_{x_{i,j,k+1}}+B^{n}_{x_{i,j+1,k}}+B^{n}_{x_{i,j,k}}\right)\\ -CB_x\left(E^{n}_{z_{i,j+1,k+1}}+E^{n}_{z_{i,j+1,k}}-E^{n}_{z_{i,j,k+1}}-E^{n}_{z_{i,j,k}}\right)\\ +CQ_x\left(E^{n}_{y_{i,j+1,k+1}}+E^{n}_{y_{i,j+1,k}}-E^{n}_{y_{i,j,k+1}}-E^{n}_{y_{i,j,k}}\right)\end{cases} \tag{9}$$

$$H^{n+1}_{x_{i,j,k}}-D2_x\cdot B^{n+1}_{x_{i,j,k}} = D1_x\cdot H^{n}_{x_{i,j,k}}-D3_x\cdot B^{n}_{x_{i,j,k}} \tag{10}$$

where

$$CA_x = \frac{2k_y-\frac{\sigma_y}{\varepsilon_0}\Delta t}{2k_y+\frac{\sigma_y}{\varepsilon_0}\Delta t}\ CB_x = \frac{\Delta t}{\left(k_y+\frac{\sigma_y}{2\varepsilon_0}\Delta t\right)\Delta y}$$

$$C1_x = \frac{\frac{k_z}{\Delta t}-\frac{\sigma_z}{2\varepsilon_0}}{\frac{k_z}{\Delta t}+\frac{\sigma_z}{2\varepsilon_0}} C2_x = \frac{\frac{k_x}{\Delta t}+\frac{\sigma_x}{2\varepsilon_0}}{\frac{\varepsilon_1 k_z}{\Delta t}+\frac{\varepsilon_1\sigma_z}{2\varepsilon_0}} C3_x = \frac{\frac{k_x}{\Delta t}-\frac{\sigma_x}{2\varepsilon_0}}{\frac{\varepsilon_1 k_z}{\Delta t}+\frac{\varepsilon_1\sigma_z}{2\varepsilon_0}}$$

$$CP_x = \frac{k_y-\frac{\sigma_{ym}}{\varepsilon_0}\Delta t}{k_y+\frac{\sigma_{ym}}{\varepsilon_0}\Delta t}\ CQ_x = \frac{\Delta t}{\left(k_y+\frac{\sigma_{ym}}{2\varepsilon_0}\Delta t\right)\Delta y}$$

$$D1_x = \frac{\frac{k_z}{\Delta t}-\frac{\sigma_{zm}}{2\varepsilon_0}}{\frac{k_z}{\Delta t}+\frac{\sigma_{zm}}{2\varepsilon_0}} D2_x = \frac{\frac{k_x}{\Delta t}+\frac{\sigma_{xm}}{2\varepsilon_0}}{\frac{\mu_1 k_z}{\Delta t}+\frac{\mu_1\sigma_{zm}}{2\varepsilon_0}}$$

$$D3_x = \frac{\frac{k_x}{\Delta t}-\frac{\sigma_{xm}}{2\varepsilon_0}}{\frac{\mu_1 k_z}{\Delta t}+\frac{\mu_1\sigma_{zm}}{2\varepsilon_0}}.$$

From the above system of equations, it is evident that solving the discretized scheme in its current form requires treating it as a linear system, involving the assembly of coefficient matrices and the solution of coupled field variables through direct matrix operations. However, this approach presents two major drawbacks as follows.

1) The computation of the coefficient matrix is highly intensive, demanding substantial memory, and resulting in slow solution speed.

2) More critically, the present work is built upon an MS Preissmann scheme combined with a LOD operator splitting

strategy [25]. Solving the system via a coefficient matrix would not be compatible with this approach and may lead to undesirable effects. Therefore, the UPML absorbing boundary proposed in this work must also be decomposed using the LOD method.

To address these issues and ensure compatibility with the proposed LOD-based MS-FDTD framework, the UPML formulation must also be decomposed using the LOD technique, in the same manner as the transformation from FDTD to LOD-FDTD. After applying the LOD scheme, the original set of 12 coupled equations is split into 24 directional subequations. For instance, (7) is decomposed into (13) and (14). Similar to the earlier part, for clarity, only one representative set of field components is presented below

$$E^{n+\frac{1}{2}}_{x_{i,j,k}} = C1_{xy_{i,j,k}} \cdot E^{n}_{x_{i,j,k}} + C2_{xy_{i,j,k}} \cdot D^{n+\frac{1}{2}}_{x_{i,j,k}} - C3_{xy_{i,j,k}} \cdot D^{n}_{x_{i,j,k}} \tag{11}$$

$$E^{n+1}_{x_{i,j,k}} = C1_{xz_{i,j,k}} \cdot E^{n+\frac{1}{2}}_{x_{i,j,k}} + C2_{xz_{i,j,k}} \cdot D^{n+1}_{x_{i,j,k}} - C3_{xz_{i,j,k}} \cdot D^{n+\frac{1}{2}}_{x_{i,j,k}} \tag{12}$$

$$\begin{cases} D^{n+\frac{1}{2}}_{x_{i,j+1,k}} + D^{n+\frac{1}{2}}_{x_{i,j,k}} = CA_{xy_{i,j+1,k}} D^{n}_{x_{i,j+1,k}} + CA_{xy_{i,j,k}} D^{n}_{x_{i,j,k}} \\ + CB_{xy_{i,j+1,k}} \left(H^{n+1}_{z_{i,j+1,k}} + H^{n+\frac{1}{2}}_{z_{i,j+1,k}} \right) - CB_{xy_{i,j,k}} \left(H^{n+1}_{z_{i,j,k}} + H^{n+\frac{1}{2}}_{z_{i,j,k}} \right) \end{cases} \tag{13}$$

$$\begin{cases} D^{n+1}_{x_{i,j,k+1}} + D^{n+1}_{x_{i,j,k}} = CA_{xz_{i,j,k+1}} D^{n+\frac{1}{2}}_{x_{i,j,k+1}} + CA_{xz_{i,j,k}} D^{n+\frac{1}{2}}_{x_{i,j,k}} \\ - CB_{xz_{i,j,k+1}} \left(H^{n+1}_{y_{i,j,k+1}} + H^{n+\frac{1}{2}}_{y_{i,j,k+1}} \right) - CB_{xz_{i,j,k}} \left(H^{n+1}_{y_{i,j,k}} + H^{n+\frac{1}{2}}_{y_{i,j,k}} \right) \end{cases} \tag{14}$$

$$H^{n+\frac{1}{2}}_{x_{i,j,k}} = D1_{xy_{i,j,k}} \cdot H^{n}_{x_{i,j,k}} + D2_{xy_{i,j,k}} \cdot B^{n+\frac{1}{2}}_{x_{i,j,k}} - D3_{xy_{i,j,k}} \cdot B^{n}_{x_{i,j,k}} \tag{15}$$

$$H^{n+1}_{x_{i,j,k}} = D1_{xz_{i,j,k}} \cdot H^{n+\frac{1}{2}}_{x_{i,j,k}} + D2_{xz_{i,j,k}} \cdot B^{n+1}_{x_{i,j,k}} - D3_{xz_{i,j,k}} \cdot B^{n+\frac{1}{2}}_{x_{i,j,k}} \tag{16}$$

$$\begin{cases} B^{n+\frac{1}{2}}_{x_{i,j+1,k}} + B^{n+\frac{1}{2}}_{x_{i,j,k}} = CP_{xy_{i,j+1,k}} B^{n}_{x_{i,j+1,k}} + CP_{xy_{i,j,k}} B^{n}_{x_{i,j,k}} \\ - CQ_{xy_{i,j+1,k}} \left(E^{n+1}_{z_{i,j+1,k}} + E^{n+\frac{1}{2}}_{z_{i,j+1,k}} \right) + CQ_{xy_{i,j+1,k}} \left(E^{n+1}_{z_{i,j,k}} + E^{n+\frac{1}{2}}_{z_{i,j,k}} \right) \end{cases} \tag{17}$$

$$\begin{cases} B^{n+1}_{x_{i,j,k+1}} + B^{n+1}_{x_{i,j,k}} = CP_{xz_{i,j,k+1}} B^{n+\frac{1}{2}}_{x_{i,j,k+1}} + CP_{xz_{i,j,k}} B^{n+\frac{1}{2}}_{x_{i,j,k}} \\ + CQ_{xz_{i,j,k+1}} \left(E^{n+1}_{y_{i,j,k+1}} + E^{n+\frac{1}{2}}_{y_{i,j,k+1}} \right) - CQ_{xz_{i,j,k}} \left(E^{n+1}_{y_{i,j,k}} + E^{n+\frac{1}{2}}_{y_{i,j,k}} \right) \end{cases} \tag{18}$$

$$H^{n+1}_{z_{i,j,k}} = D1_{zy_{i,j,k}} \cdot H^{n+\frac{1}{2}}_{z_{i,j,k}} + D2_{zy_{i,j,k}} \cdot B^{n+1}_{z_{i,j,k}} - D3_{zy_{i,j,k}} \cdot B^{n+\frac{1}{2}}_{z_{i,j,k}} \tag{19}$$

$$\begin{cases} B^{n+1}_{z_{i,j+1,k}} + B^{n+1}_{z_{i,j,k}} = CP_{zy_{i,j+1,k}} B^{n}_{z_{i,j+1,k}} + CP_{zy_{i,j,k}} B^{n}_{z_{i,j,k}} \\ - CQ_{zy_{i,j+1,k}} \left(E^{n}_{x_{i,j+1,k}} + E^{n+\frac{1}{2}}_{x_{i,j+1,k}} \right) + CQ_{zy_{i,j+1,k}} \left(E^{n}_{x_{i,j,k}} + E^{n+\frac{1}{2}}_{x_{i,j,k}} \right) \end{cases} \tag{20}$$

where

$$CB_{xy} = \frac{4\Delta t}{\left(4k_y + \frac{\sigma_y}{\varepsilon_0}\Delta t\right)\Delta y} CA_{xy} = \frac{4k_y - \frac{\sigma_y}{\varepsilon_0}\Delta t}{4k_y + \frac{\sigma_y}{\varepsilon_0}\Delta t}$$

$$CP_{xy} = \frac{4k_y - \frac{\sigma_{ym}}{\varepsilon_0}\Delta t}{4k_y + \frac{\sigma_{ym}}{\varepsilon_0}\Delta t} CQ_{xy} = \frac{4\Delta t}{\left(4k_y + \frac{\sigma_{ym}}{\varepsilon_0}\Delta t\right)\Delta y}$$

$$CA_{xz} = C1_{xy} = 1 CP_{xz} = D1_{xy} = 1$$

$$CB_{xz} = CQ_{xz} = \frac{\Delta t}{\Delta y} C2_{xy} = C3_{xy} = \frac{1}{\varepsilon_1}$$

$$D2_{xy} = D3_{xy} = \frac{1}{\mu_1} D1_{xz} = \frac{\frac{2k_z}{\Delta t} - \frac{\sigma_{zm}}{2\varepsilon_0}}{\frac{2k_z}{\Delta t} + \frac{\sigma_{zm}}{2\varepsilon_0}}$$

$$C2_{xy} = C3_{xy} = \frac{2/\Delta t}{\frac{2\varepsilon_1 k_z}{\Delta t} + \frac{\varepsilon_1 \sigma_z}{2\varepsilon_0}} C1_{xz} = \frac{\frac{2k_z}{\Delta t} - \frac{\sigma_z}{2\varepsilon_0}}{\frac{2k_z}{\Delta t} + \frac{\sigma_z}{2\varepsilon_0}}$$

$$D2_{xz} = D3_{xz} = \frac{2/\Delta t}{\frac{2\mu_1 k_z}{\Delta t} + \frac{\mu_1 \sigma_{zm}}{2\varepsilon_0}}.$$

In conventional explicit FDTD algorithms, the UPML absorbs outgoing waves by introducing stretched-coordinate variables *Sx*, *Sy*, and *Sz* along the respective spatial directions. At corners and edges, where multiple stretching directions are simultaneously active, the effective damping is achieved by the product of the stretching factors (e.g., *Sx* and *Sy*), which is directly incorporated into the update equations. This process is straightforward and does not require any special additional treatment beyond multiplying the factors.

In the proposed LOD–MS framework, the global update process is decomposed into directional substeps, each involving only the partial derivative and its corresponding stretching parameter (e.g., $1/Sx$). Through the sequential execution of these substeps, the damping contributions from different coordinate directions are naturally accumulated. As a result, the same product effect of stretching parameters in corner regions emerges implicitly, without the need to explicitly construct cross terms. This cumulative absorption can be interpreted as a structured numerical composition. Each LOD subupdate serves as a directional operator contributing partial attenuation, and when composed over one full time step, these operators recover the multidimensional absorption behavior consistent with conventional UPML. Hence, no special edge or corner treatment is required, and the physical absorption effect arises directly from the algorithmic structure.

This can be observed in (11)–(18), where the update coefficients are significantly simplified compared to the unsplit system. Each directional subcomponent absorbs waves independently in its respective direction, and their composition ensures effective absorption in multidimensional settings. This property enhances algorithmic elegance, avoids the need for manually constructed cross terms, and is highly compatible with the Preissmann-type MS formulation under LOD decomposition. As a result, the proposed scheme offers improved numerical stability, ease of implementation, and scalability while maintaining excellent absorption performance at boundaries and corners.

As shown in (11), (13), (19), and (20), the UPML formulation remains implicit even after applying the LOD splitting scheme. To facilitate efficient numerical implementation, additional algebraic manipulations are required. Specifically, (13) and (20) are first substituted into (11) and (19), respectively, yielding an intermediate expression similar to (22) as shown at the bottom of the next page. Subsequently, the transformed version of (13) is further substituted into (11), followed by appropriate simplifications, resulting in an implicit tridiagonal update formulation denoted as (21) as shown at the bottom of the next page.

Similarly, (23)), as shown at the bottom of the next page, is obtained using the same substitution procedure. By simultaneously solving the system composed of (21) and (22), the field component in a single spatial direction can be obtained. The update equations for the other spatial components can be derived in the same manner. For illustration, the update formulas for the *Ex* component in two different directions are presented below.

where

$$B = \frac{C2_K CB_K}{C2_{K+1}CB_{K+1} + C2_K CB_K}$$

$$A = \frac{C2_{K-1}CB_{K-1}}{C2_{K-1}CB_{K-1} + C2_K CB_K}.$$

In the above equations, only the varying subscripts in the coefficients are explicitly shown for clarity. The symbols A and B contain direction-dependent terms, where the subscript K is one of the spatial directions (x, y, and z). The exact form of the coefficients in A and B should be selected according to the current direction under consideration during the update process. Fig. 1 shows the flowchart of the proposed MS-FDTD method with integrated UPML treatment. During each iteration, the electric and magnetic fields are updated in a directionally split manner based on the LOD scheme. Notably, transitioning from the original MS-FDTD method to its UPML-extended version requires only modifying the coefficients in the tridiagonal matrices. All UPML-related damping parameters are embedded during initialization, and no additional UPML-specific processing is needed during the time-stepping procedure.

III. NUMERICAL STABILITY

The later part utilize the Fourier method to analyze the stability of the algorithm proposed in this article. The matrix in the spatial spectral domain between the nth time step and the next $(n+1)$th time step is rewritten using the plane-wave solution of Maxwell's system of equations

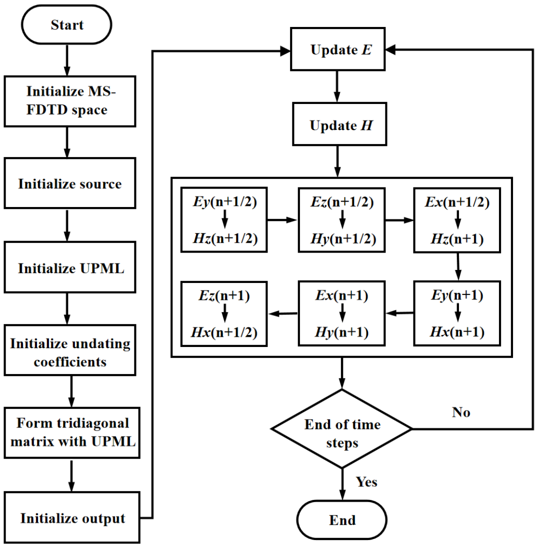

Fig. 1. Flowchart of iteration for the MS-FDTD-UPML method.

$$\psi^{n+1} = \mathbf{\Lambda}\psi^n = \mathrm{A}^{-1}\mathrm{B}\psi^n = \mathrm{C}^{-1}\mathrm{D}\psi^n. \tag{25}$$

Applying the discrete Fourier transform and assuming a plane-wave solution of the form

$$Z^n = Z_0 e^{j(nk\Delta x - \omega n\Delta t)}. \tag{26}$$

$$\begin{cases} B\cdot E^{\mathrm{n}+\frac{1}{2}}_{x_{i,j+1,k}} + (B-A+1)\,E^{\mathrm{n}+\frac{1}{2}}_{x_{i,j,k}} + (1-A)\,E^{\mathrm{n}+\frac{1}{2}}_{x_{i,j-1,k}} - B\cdot C2_{x_{j+1}}CB_{x_{j+1}}D2_{z_{j+1}}CQ_{z_{j+1}}\cdot E^{\mathrm{n}+\frac{1}{2}}_{x_{i,j+1,k}} \\ -\ \left(B\cdot C2_{x_{j+1}}CB_{x_{j+1}}D2_{z_j}CQ_{z_j} + A\cdot C2_{x_j}CB_{x_j}D2_{z_j}CQ_{z_j}\right)E^{\mathrm{n}+\frac{1}{2}}_{x_{i,j,k}} + A\cdot C2_{x_j}CB_{x_j}D2_{z_{j-1}}CQ_{z_{j-1}}E^{\mathrm{n}+\frac{1}{2}}_{x_{i,j-1,k}} \\ = B\cdot CA_{x_{j+1}}E^{\mathrm{n}}_{x_{i,j+1,k}} + CA_{x_j}(B-A+1)\,E^{\mathrm{n}}_{x_{i,j,k}} + CA_{x_{j-1}}(1-A)\,E^{\mathrm{n}}_{x_{i,j-1,k}} + B\cdot C2_{x_{j+1}}CB_{x_{j+1}}D2_{z_{j+1}}CQ_{z_{j+1}}E^{\mathrm{n}}_{x_{i,j+1,k}} \\ +\ \left(B\cdot C2_{x_{j+1}}CB_{x_{j+1}}D2_{z_j}CQ_{z_j} + A\cdot C2_{x_j}CB_{x_j}D2_{z_j}CQ_{z_j}\right)E^{\mathrm{n}}_{x_{i,j,k}} + A\cdot C2_{x_j}CB_{x_j}D2_{z_{j-1}}CQ_{z_{j-1}}E^{\mathrm{n}}_{x_{i,j-1,k}} \\ -\ \left(B\cdot C2_{x_{j+1}}CB_{x_{j+1}}C1_{z_{j+1}}H^{n+\frac{1}{2}}_{z_{i,j+1,k}} + \left(B\cdot C2_{x_{j+1}}CB_{x_{j+1}}C1_{z_j} - A\cdot C2_{x_j}CB_{x_j}C1_{z_j}\right)H^{n+\frac{1}{2}}_{z_{i,j,k}} - \left(A\cdot C2_{x_j}CB_{x_j}C1_{z_{j-1}}\right)H^{n+\frac{1}{2}}_{z_{i,j-1,k}}\right) \\ -\ \left(B\cdot C2_{x_{j+1}}CB_{x_{j+1}}H^{n+\frac{1}{2}}_{z_{i,j+1,k}} + C2_{x_j}CB_{x_j}(1-B-A)\,H^{n+\frac{1}{2}}_{z_{i,j,k}} - C2_{x_{j-1}}CB_{x_{j-1}}\cdot(1-A)\,H^{n+\frac{1}{2}}_{z_{i,j-1,k}}\right) \end{cases} \tag{21}$$

$$\begin{aligned} H^{n+1}_{z_{i,j,k}} + H^{n+1}_{z_{i,j+1,k}} &= D1_{\mathrm{zy}_{j+1}}\cdot H^n_{z_{i,j+1,k}} + D1_{\mathrm{zy}_j}\cdot H^n_{z_{i,j,k}} + D2_{zy_{i,j+1,k}}CQ_{zy_{i,j+1,k}}\cdot\left(E^{n+\frac{1}{2}}_{x_{i,j+1,k}} + E^n_{x_{i,j+1,k}}\right) - D2_{zy_{i,j,k}}CQ_{zy_{i,j,k}} \\ &\quad\cdot\left(E^{n+\frac{1}{2}}_{x_{i,j,k}} + E^n_{x_{i,j+1,k}}\right) \end{aligned} \tag{22}$$

$$\begin{cases} \left(B\cdot E^{\mathrm{n}+1}_{x_{i,j,k+1}} + (B-A+1)\,E^{\mathrm{n}+1}_{x_{i,j,k}} + (1-A)\,E^{\mathrm{n}+1}_{x_{i,j,k-1}}\right) - B\cdot C2_{x_{k+1}}CB_{x_{k+1}}D2_{y_{k+1}}CQ_{y_{k+1}}\cdot E^{\mathrm{n}+1}_{x_{i,j,k+1}} \\ -\ \left(B\cdot C2_{x_{k+1}}CB_{x_{k+1}}D2_{y_{k+1}}CQ_{y_{k+1}} + A\cdot C2_{x_k}CB_{x_k}D2_{y_k}CQ_{y_k}\right)E^{\mathrm{n}+1}_{x_{i,j,k}} + A\cdot C2_{x_k}CB_{x_k}D2_{y_{k-1}}CQ_{y_{k-1}}E^{\mathrm{n}+1}_{x_{i,j-1,k}} \\ = B\cdot C1_{x_{k+1}}E^{\mathrm{n}+\frac{1}{2}}_{x_{i,j,k+1}} + C1_{x_{k+1}}(B-A+1)\,E^{\mathrm{n}+\frac{1}{2}}_{x_{i,j,k}} + C1_{x_k}(1-A)\,E^{\mathrm{n}+\frac{1}{2}}_{x_{i,j,k-1}} + B\cdot C2_{x_{k+1}}CB_{x_{k+1}}D2_{y_{k+1}}CQ_{y_{k+1}}E^{\mathrm{n}+\frac{1}{2}}_{x_{i,j,k+1}} \\ +\ \left(B\cdot C2_{x_{k+1}}CB_{x_{k+1}}D2_{y_{k+1}}CQ_{y_{k+1}} + A\cdot C2_{x_k}CB_{x_k}D2_{y_k}CQ_{y_k}\right)E^{\mathrm{n}+\frac{1}{2}}_{x_{i,j,k}} + A\cdot C2_{x_k}CB_{x_k}D2_{y_{k-1}}CQ_{y_{k-1}}E^{\mathrm{n}+\frac{1}{2}}_{x_{i,j,k-1}} \\ -\ \left(B\cdot C2_{x_{k+1}}CB_{x_{k+1}}CP_{y_{k+1}}H^{n+\frac{1}{2}}_{y_{i,j,k+1}} + \left(B\cdot C2_{x_{k+1}}CB_{x_{k+1}}CP_{y_k} - A\cdot C2_{x_k}CB_{x_k}CP_{y_k}\right)H^{n+\frac{1}{2}}_{y_{i,j,k}} - \left(A\cdot C2_{x_k}CB_{x_k}CP_{y_{k-1}}\right)H^{n+\frac{1}{2}}_{y_{i,j,k-1}}\right) \\ -\ \left(B\cdot C2_{x_{k+1}}CB_{x_{k+1}}H^{n+\frac{1}{2}}_{y_{i,j,k+1}} + C2_{x_k}CB_{x_k}(1-B-A)\,H^{n+\frac{1}{2}}_{y_{i,j,k}} - C2_{x_{k-1}}CB_{x_{k-1}}\cdot(1-A)\,H^{n+\frac{1}{2}}_{y_{i,j,k-1}}\right) \end{cases} \tag{23}$$

$$\begin{aligned} H^{n+1}_{y_{i,j,k}} + H^{n+1}_{y_{i,j,k+1}} &= CP_{\mathrm{yz}_k}\cdot H^{n+\frac{1}{2}}_{z_{i,j,k}} + CP_{\mathrm{yz}_{k+1}}\cdot H^{n+\frac{1}{2}}_{z_{i,j,k+1}} \\ &\quad - \left(D2_{yz_{k+1}}CQ_{yz_{k+1}}\cdot\left(E^{n+1}_{x_{i,j,k+1}} + E^n_{x_{i,j,k+1}}\right) - D2_{yz_k}CQ_{yz_k}\cdot\left(E^{n+1}_{x_{i,j,k}} + E^n_{x_{i,j,k}}\right)\right) \end{aligned} \tag{24}$$

We substitute this form into the difference equation to obtain the corresponding eigenvalue equation

$$\lambda Z_0 = \mathrm{G}Z_0. \tag{27}$$

The stability analysis of the MS-FDTD scheme is initially performed by matrixing all the coefficients in (7)–(10), and then substituting the plane-wave solution of Maxwell's system of equations into the matrix to obtain the following matrices. UPML is implemented in the time domain by introducing auxiliary variables or PML stretching factors. In the time domain, this is equivalent to incorporating a conductive loss term, which introduces additional damping into the update matrix.

As a result, the spatial derivative in the original Fourier-domain update matrix is replaced by

$$\frac{\partial}{\partial x} \rightarrow \frac{1}{s_x}\frac{\partial}{\partial x}, s_x = \kappa_x + \frac{\sigma_x}{j\omega\varepsilon_0}. \tag{28}$$

After introducing the damping matrix, the original Fourier-domain update matrix is modified as follows:

$$\mathrm{A} = \begin{bmatrix} 1 & 0 & 0 & 0 & \frac{\Delta t}{s_z\varepsilon}\frac{\partial}{\partial z} & -\frac{\Delta t}{s_y\varepsilon}\frac{\partial}{\partial y} \\ 0 & 1 & 0 & -\frac{\Delta t}{s_z\varepsilon}\frac{\partial}{\partial z} & 0 & \frac{\Delta t}{s_x\varepsilon}\frac{\partial}{\partial x} \\ 0 & 0 & 1 & \frac{\Delta t}{s_y\varepsilon}\frac{\partial}{\partial y} & -\frac{\Delta t}{s_x\varepsilon}\frac{\partial}{\partial x} & 0 \\ 0 & -\frac{\Delta t}{s_z\mu}\frac{\partial}{\partial z} & \frac{\Delta t}{s_y\mu}\frac{\partial}{\partial y} & 1 & 0 & 0 \\ \frac{\Delta t}{s_z\mu}\frac{\partial}{\partial z} & 0 & -\frac{\Delta t}{s_x\mu}\frac{\partial}{\partial x} & 0 & 1 & 0 \\ -\frac{\Delta t}{s_y\mu}\frac{\partial}{\partial y} & \frac{\Delta t}{s_x\mu}\frac{\partial}{\partial x} & 0 & 0 & 0 & 1 \end{bmatrix}$$

$$\mathrm{B} = \begin{bmatrix} 1 & 0 & 0 & 0 & -\frac{\Delta t}{s_z\varepsilon}\frac{\partial}{\partial z} & \frac{\Delta t}{s_y\varepsilon}\frac{\partial}{\partial y} \\ 0 & 1 & 0 & \frac{\Delta t}{s_z\varepsilon}\frac{\partial}{\partial z} & 0 & -\frac{\Delta t}{s_x\varepsilon}\frac{\partial}{\partial x} \\ 0 & 0 & 1 & -\frac{\Delta t}{s_y\varepsilon}\frac{\partial}{\partial y} & \frac{\Delta t}{s_x\varepsilon}\frac{\partial}{\partial x} & 0 \\ 0 & \frac{\Delta t}{s_z\mu}\frac{\partial}{\partial z} & -\frac{\Delta t}{s_y\mu}\frac{\partial}{\partial y} & 1 & 0 & 0 \\ -\frac{\Delta t}{s_z\mu}\frac{\partial}{\partial z} & 0 & \frac{\Delta t}{s_x\mu}\frac{\partial}{\partial x} & 0 & 1 & 0 \\ \frac{\Delta t}{s_y\mu}\frac{\partial}{\partial y} & -\frac{\Delta t}{s_x\mu}\frac{\partial}{\partial x} & 0 & 0 & 0 & 1 \end{bmatrix}.$$

The eigenvalues of Λ are solved as

$$\lambda_1 = \lambda_2 = 1$$

$$\lambda_3 = \lambda_4 = -\frac{a - b + j\sqrt{4ab}}{b + a}$$

$$\lambda_5 = \lambda_6 = -\frac{a - b - j\sqrt{4ab}}{b + a}$$

with $a = (s_z^2 s_y^2 w_x^2 + s_x^2 s_z^2 w_y^2 + s_x^2 s_y^2 w_z^2)/(\varepsilon\mu), b = s_x^2 s_y^2 s_z^2, w_x = c\sin(k_x\Delta x/2)\Delta t/\Delta x, w_y = c\sin(k_y\Delta y/2)\Delta t/\Delta y, w_z = c\sin(k_z\Delta z/2)\Delta t/\Delta z$.

So, we can conclude that the values of every eigenvalue are equal to 1

$$|\lambda| \equiv 1.$$

Therefore, it is demonstrated that the UPML scheme in the MS-FDTD method is unconditionally stable. In this work, the UPML formulation is based on the LOD-split scheme, and thus, a separate stability analysis is required for the LOD-decomposed UPML.

Since the LOD method updates one spatial direction at a time, the stability analysis is presented here using the x-direction as an example. Initially, the derivation of the coefficient matrix follows a procedure similar to that in (11)–(18). Subsequently, by substituting the plane wave solution of the Maxwell equations, the following coefficient matrix is obtained:

$$\mathrm{C} = \begin{bmatrix} 1 & 0 & 0 & 0 & 0 & 0 \\ 0 & 1 & 0 & 0 & 0 & \frac{\Delta t}{\mathrm{s}_x\varepsilon}\frac{\partial}{\partial x} \\ 0 & 0 & 1 & 0 & -\frac{\Delta t}{\mathrm{s}_x\varepsilon}\frac{\partial}{\partial x} & 0 \\ 0 & 0 & 0 & 1 & 0 & 0 \\ 0 & 0 & -\frac{\Delta t}{\mathrm{s}_x\mu}\frac{\partial}{\partial x} & 0 & 1 & 0 \\ 0 & \frac{\Delta t}{\mathrm{s}_x\mu}\frac{\partial}{\partial x} & 0 & 0 & 0 & 1 \end{bmatrix}$$

$$\mathrm{D} = \begin{bmatrix} 1 & 0 & 0 & 0 & 0 & 0 \\ 0 & 1 & 0 & 0 & 0 & -\frac{\Delta t}{\mathrm{s}_x\varepsilon}\frac{\partial}{\partial x} \\ 0 & 0 & 1 & 0 & \frac{\Delta t}{\mathrm{s}_x\varepsilon}\frac{\partial}{\partial x} & 0 \\ 0 & 0 & 0 & 1 & 0 & 0 \\ 0 & 0 & \frac{\Delta t}{\mathrm{s}_x\mu}\frac{\partial}{\partial x} & 0 & 1 & 0 \\ 0 & -\frac{\Delta t}{\mathrm{s}_x\mu}\frac{\partial}{\partial x} & 0 & 0 & 0 & 1 \end{bmatrix}.$$

Upon solving for the eigenvalues, the following result is obtained:

$$\lambda_1 = \lambda_2 = 1$$

$$\lambda_3 = \lambda_4 = -\frac{c - d + j\sqrt{4cd}}{d + c}$$

$$\lambda_5 = \lambda_6 = -\frac{c - d - j\sqrt{4cd}}{d + c}$$

with $c = s_x^2 w_x^2/(\varepsilon\mu), w_x = c\Delta t\sin(k_x\Delta x/2)/\Delta x, d = s_x^2 x$.

Since the update equations in the y- and z-directions share the same structural form as that in the x-direction, similar eigenvalue analyses can be performed. These yield the same result, namely that the eigenvalue magnitudes in all three directions are equal to 1, confirming the unconditional stability of each directional subupdate. However, the LOD scheme sequentially decomposes the multidimensional update into independent 1-D substeps. The overall stability of the LOD–MS-FDTD scheme can be rigorously analyzed through the product of the amplification matrices of its suboperators. In this interpretation, each directional operator preserves stability individually, and their combined amplification matrix also has a spectral radius strictly equal to 1

$$\rho(G) = \rho(Gx) \cdot \rho(Gy) \cdot \rho(Gz) = 1.$$

Therefore, we conclude that the proposed MS UPML formulation maintains numerical stability under LOD splitting.

IV. NUMERICAL RESULTS

In this section, three representative test cases are presented to evaluate the effectiveness and accuracy of the proposed UPML absorbing boundary implemented within the MS-FDTD framework. An important condition used in numerical arithmetic is Courant–Friedrichs–Lewy (CFL) number (i.e., $\Delta t/\Delta t_{\mathrm{CFL}}$), where Δt_{CFL} is the maximum stability limit of the FDTD method. The computer configuration is an Intel Core i7-13700K CPU (3.40 GHz) and 64 GB RAM (DDR4 3600 MHz).

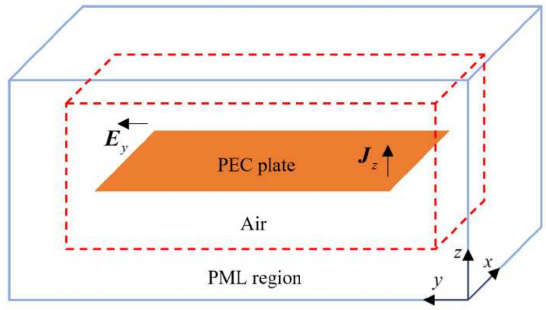

Fig. 2. Electric current dipole source and the observation point are placed at two opposite corners. The current source is located one grid cell above the PEC plate. The observation point is positioned one grid cell away from the diagonal corner of the PEC plate and two grid cells away from the inner interface of the UPML, ensuring a fixed distance relative to the PML boundary for consistent waveform comparison.

A. Reflection Error Analysis of PEC Plate

As illustrated in Fig. 2, the entire simulation domain is discretized into a grid of size 200 × 200 × 50 cells. A perfectly electrically conducting (PEC) plate, modeled as an ideal zero-thickness surface with dimensions 50 × 100 cells, is placed within the domain. All boundaries of the computational domain are terminated with UPML to absorb outgoing waves.

The excitation source is defined as

$$I(t) = -2 \cdot \frac{(t - t_0)}{t_\omega} e^{-\left(\frac{t-t_0}{t_\omega}\right)^2} \tag{29}$$

where $t_\omega = 3.33e^{-12}$ s and $t_0 = 4\ t_\omega$. $I(t)$ is the impressed current density in the source region, aligned with the electric field component being updated, and is introduced into the discrete formulation as the external excitation term corresponding to (1). The spatial grid resolution is set to $\Delta x = \Delta y = \Delta z = 1e^{-4}$ m, and the time step is adjusted according to the CFLN number under investigation. To quantitatively assess the absorption performance of the UPML, the relative reflection error is calculated using (30). The reference solution is obtained from a simulation with an enlarged computational domain and significantly thickened UPML layers, which effectively suppress boundary reflections within the time window of interest, and thus, provide a practical approximation to a reflection-free case

$$\text{Error}^n_{i,j,k} = 20\log_{10}\frac{\left\|E^n_{i,j,k} - E^n_{\text{REF}i,j,k}\right\|}{\left\|E_{\text{REF}^n_{\max_{i,j,k}}}\right\|}. \tag{30}$$

As shown in Fig. 2, a monitoring point is selected near the lower right corner of the computational domain, located two grid cells away from the inner interface of the UPML (i.e., the boundary between the computational domain and the PML). Using the previously defined formula, the relative reflection error at this point is computed, and the results are presented in Fig. 3. It can be observed that the relative error decreases rapidly as the simulation progresses, which is consistent with the expected behavior of PML-type boundaries. This confirms that the proposed UPML retains its effectiveness when incorporated into the MS-FDTD framework.

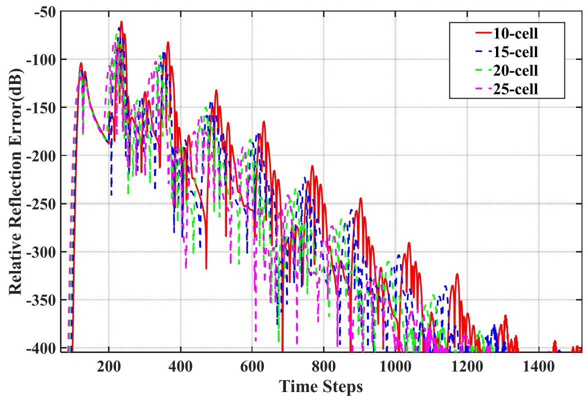

Fig. 3. Relative reflection error curves under different numbers of UPML layers.

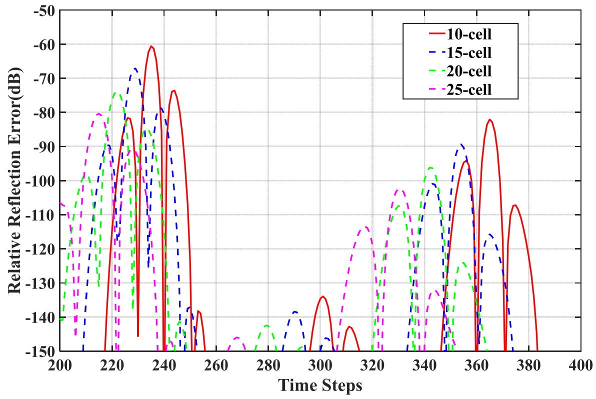

Fig. 4. Magnified view of the relative reflection error curves for different UPML layer configurations.

TABLE I

MAXIMUM RELATIVE REFLECTION ERROR OF THE PROPOSED MS-UPML METHOD UNDER DIFFERENT CFLN VALUES

CFLN	1	1.4	2	3.5	5	7
Max relative reflection error(dB)	-61.1	-61.2	-61.6	-62.9	-64.3	-66.4

Since Fig. 3 does not clearly reveal the detailed absorption characteristics, a local magnification is provided in Fig. 4 by enlarging the region around the maximum reflection error. This enables a more intuitive assessment of the UPML's performance. Both Figs. 3 and 4 compare the performance of different UPML layer thicknesses. The results clearly show that increasing the number of UPML layers significantly improves the absorption, with the relative reflection error dropping below −60 dB when the UPML is ten layers thick. Furthermore, the time step at which the peak reflection occurs varies with the number of UPML layers. This shift arises because the observation point is fixed relative to the inner PML boundary, so when the PML thickness increases, the total propagation distance from the source to the observation point decreases, leading to a change in the arrival time of the wave, and thus, the location of the peak reflection.

To verify the stability and absorption performance of the proposed structure-preserving MS UPML method under varying time-step conditions, a series of numerical simulations is conducted with CFLN numbers ranging from 1 to 7. For

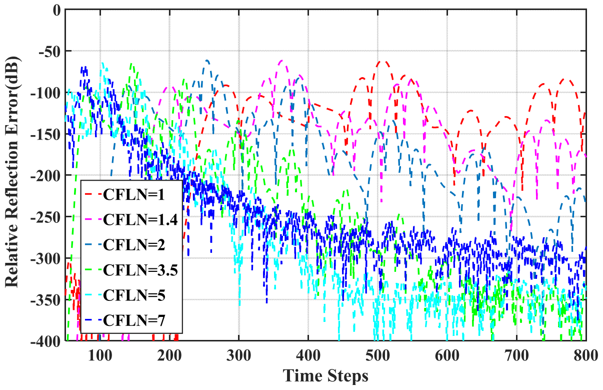

Fig. 5. Relative reflection error curves for CFL numbers ranging from 1 to 7. The horizontal axis represents the number of time steps rather than the physical time.

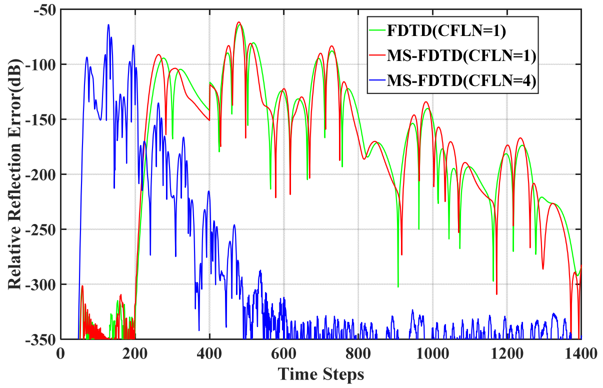

Fig. 6. Comparison of relative reflection errors between the conventional FDTD method and the proposed MS-FDTD method under the same simulation conditions.

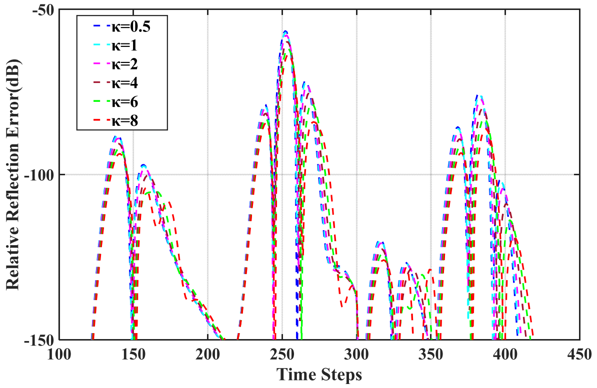

Fig. 7. Relative reflection error under oblique incidence for different values of κ.

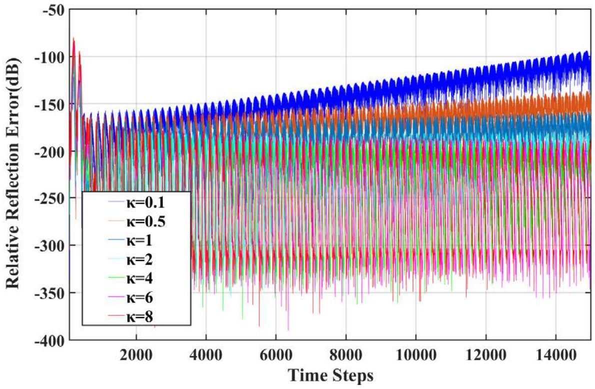

Fig. 8. Relative reflection error under normal incidence for different values of κ.

all simulations, the same computational domain, identical absorbing layer thickness (ten cells), and fixed observation point distance from the PML boundary were maintained. As shown in Fig. 5, the relative reflection errors remain below −60 dB for all CFLN values, with detailed parameters listed in Table I. This confirms that the proposed MS-FDTD method preserves its MS structure within the PML region, as the reflection error remains bounded even for large CFLNs. It should be noted, however, that excessively large CFLN values may reduce numerical accuracy and introduce waveform trailing effects, a typical characteristic of implicit FDTD-type schemes. However, as the CFL number further increases, temporal dispersion errors dominate, and the reflection error eventually rises. In Fig. 6, we provide a direct comparison between the proposed MS-FDTD method and the conventional FDTD method. Specifically, the results for MS-FDTD with CFLN = 1 and CFLN = 4 are both included, along with FDTD at CFLN = 1, enabling a fair evaluation of both accuracy and efficiency. The results show that, when CFLNs are equal, the absorption performance of MS-FDTD is nearly identical to FDTD, though at late times the classical FDTD exhibits slightly lower error due to reduced temporal dispersion. It should also be noted that although MS-FDTD with CFLN = 1 is less efficient than conventional FDTD, the ability of MS-FDTD to operate stably at larger CFLNs (e.g., CFLN = 4) allows it to retain good accuracy while achieving slightly higher computational efficiency than FDTD. These results demonstrate that the proposed method exhibits strong numerical robustness, maintains consistent absorption performance, and achieves improved computational efficiency through the relaxed time-step constraint permitted by the MS structure.

To investigate the response of the proposed MS UPML to varying incidence angles and its sensitivity to the κ parameter, two distinct scenarios were examined: one involving oblique incidence generated by a point source, and the other involving normal incidence of a plane wave. In each case, the κ parameter is varied to analyze its effect on the relative reflection error. As shown in Fig. 7, for oblique incidence, increasing κ from 0.5 to 8 resulted in a monotonic reduction in reflection error, with the best performance observed at $\kappa = 8$, where the reflection error reached a minimum of −65 dB. This trend indicates that a larger κ enhances the gradual impedance transition, leading to more effective suppression of boundary reflections. In contrast, as illustrated in Fig. 8, under normal incidence conditions, the absorption performance exhibits an opposite dependence: decreasing κ significantly improves the absorption. When κ is reduced from 8 to 0.1, the reflection error drops from approximately −90 dB to as low as −130 dB, suggesting that smaller κ values are more effective for normally incident waves. These findings highlight that the κ parameter plays a critical role in tuning the absorption characteristics depending on the wave incidence

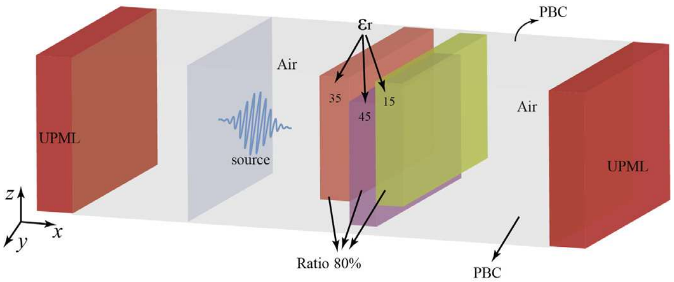

Fig. 9. Computational model of medium includes the Gaussian source propagating along the x-direction, with periodic boundaries in the y- and z-directions. The model also includes three types of media.

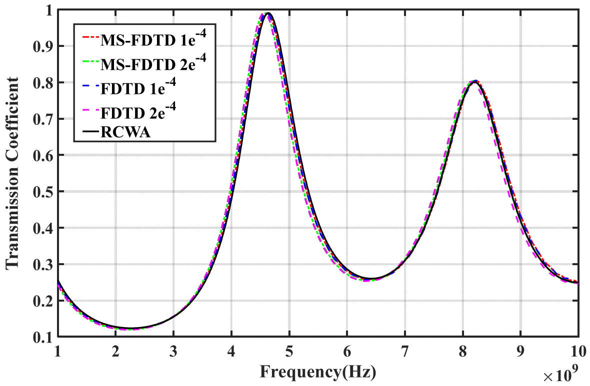

Fig. 10. Comparison of numerical and analytical results for transmission coefficient calculation in the FDTD method, the MS-FDTD method, and RCWA under different spatial resolutions.

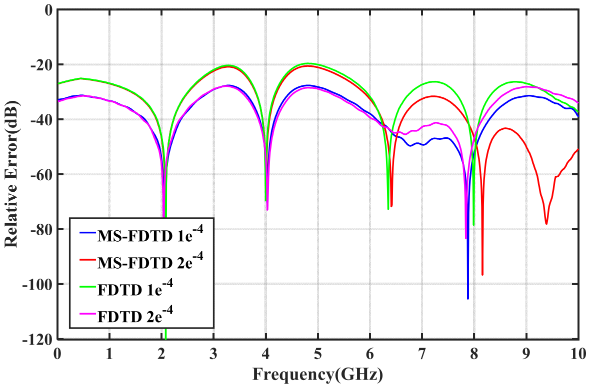

Fig. 11. Relative error comparison between the MS-FDTD method and RCWA, and the FDTD method and RCWA under different spatial resolutions.

angle. However, the method maintains stable performance over long simulation durations. The proposed MS UPML not only provides excellent overall absorption performance but also demonstrates strong directional adaptability, enabling efficient and stable boundary absorption tailored to different wave propagation scenarios.

B. *Transmission of Multilayer Dielectric Slabs*

To further validate the numerical accuracy and absorption performance of the proposed MS-FDTD method under UPML boundary conditions, as illustrated in Fig. 9, a three-layer periodic dielectric structure is constructed to simulate electromagnetic wave propagation and transmission. The simulation domain consists of a grid of size 110 × 20 × 20 cells, with periodic boundary conditions (PBCs) applied along the y- and z-directions. A Gaussian pulse is launched along the x-direction, where ten-cell UPML absorbing boundaries are applied at both ends to prevent reflections.

The dielectric region is composed of three layers with relative permittivities of 35, 45, and 15, respectively. To better approximate realistic complex materials, each layer consists of a mixture of dielectric and air with a volume ratio of 8:2, arranged in an interleaved pattern. The thickness of each dielectric layer is $2.4e^{-3}$ m. This configuration serves as a representative frequency-domain benchmark for evaluating the method's performance in multilayer systems with strong interference and frequency-selective behavior. Two spatial resolutions were tested for comparison between the conventional FDTD method and the proposed MS-FDTD method, with cell dimensions of $1e^{-4}$ and $2e^{-4}$ m. The CFLN number is set to 5 for the MS-FDTD method and 1 for the conventional FDTD method to satisfy their respective stability conditions. At the higher resolution setting ($\Delta x = \Delta y = \Delta z = 1e^{-4}$ m), Fig. 10 presents the transmission coefficients computed by the MS-FDTD method and the FDTD method, compared against a reference solution obtained using the rigorous coupled-wave analysis (RCWA) method. As observed, both the FDTD method and the MS-FDTD method results show excellent agreement with the RCWA reference. To more clearly illustrate the differences between the methods, Fig. 11 presents the corresponding relative error, defined as $20\log_{10}(|T_1 - T_0|/T_0)$, where T_1 represents the transmission coefficient results calculated by the MS-FDTD method, the FDTD method, and T_0 represents the transmission coefficient results calculated by RCWA.

Under the high-resolution configuration, the MS-FDTD method exhibits a slight advantage over the FDTD method in the high-frequency range. To further highlight the difference in spectral resolution, the spatial step size is increased to $2e^{-4}$ m, while all other parameters were kept unchanged. The corresponding transmission results and relative errors are also shown in Fig. 11. In this lower resolution case, both methods remain consistent in the low-frequency range, but the MS-FDTD method clearly outperforms the FDTD method in the high-frequency regime, with significantly reduced error. The MS-FDTD method employs a more relaxed CFL condition, which, although incurring a relatively higher computational cost per iteration, utilizes the Thomas algorithm for efficiently solving tridiagonal systems. As a result, the simulation is completed in 70.06 s, which is notably faster than the conventional FDTD method (103.57 s). These results indicate that the MS-FDTD method not only maintains high accuracy under fine discretization but also preserves superior resolution in the high-frequency range when the spatial discretization is coarse. This robustness in resolving fine spectral details demonstrates the method's strong potential for accurately capturing complex electromagnetic propagation phenomena.

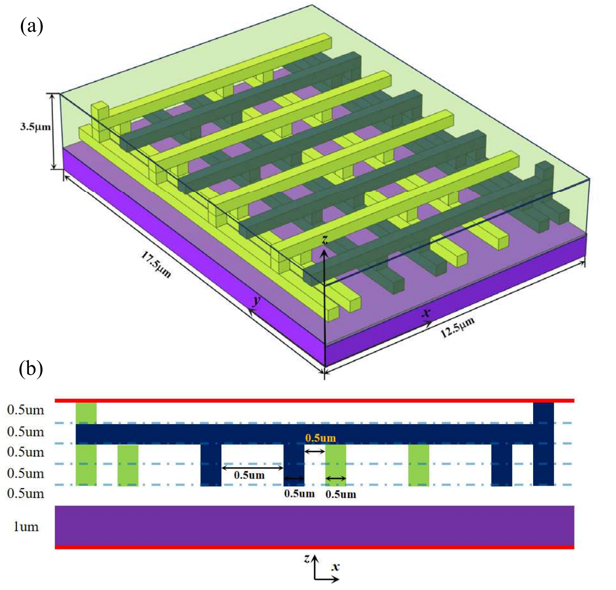

Fig. 12. Structural diagram of the 3-D on-chip power grid model (a) overall view and (b) section view.

TABLE II

Simulation Steps and Simulation Time

	FDTD	MS-FDTD
Time Step (s)	4.84×10^{-16}	1.45×10^{-15}
Number of Iterations	20000	6667
Simulation Time (s)	258.46	156.45
Memory	14.7MB	30.3MB

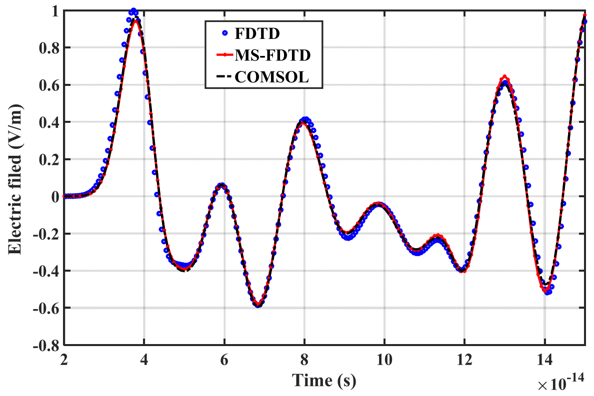

Fig. 13. Electric field amplitude after passing through the 3-D chip.

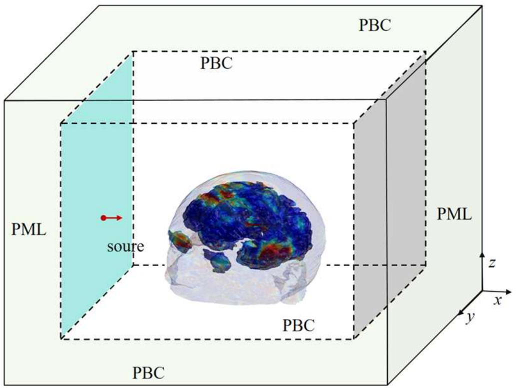

Fig. 14. 3-D human brain model.

C. Power Distribution Network

To further evaluate the adaptability and practical applicability of the proposed MS-FDTD method in complex real-world structures, two representative 3-D models are presented below: a 3-D chip structure and a human brain tissue model. The geometric configuration of the power grid in the 3-D chip is illustrated in Fig. 12. The interconnects are made of copper (with a relative permittivity of 1), surrounded by silicon dioxide (relative permittivity 3.9), and the substrate is composed of silicon (relative permittivity 13.9). The computational domain consists of 70 × 50 × 14 cells, with ten-layer UPML absorbing boundaries applied in all *x*-, *y*-, and *z*-directions. A point source is placed outside the model to excite the field, while electric field magnitudes are recorded at an observation point located inside the structure. The spatial resolution is uniformly set to $2.5e^{-7}$ m. For time stepping, the MS-FDTD method employs a time step of $1.45e^{-15}$s (CFLN = 3), whereas the conventional FDTD method uses $4.84e^{-16}$ s (CFLN = 1)—approximately half the MS-FDTD step size—allowing the MS-FDTD to improve computational efficiency while maintaining numerical stability. To assess accuracy, simulation results from both methods are compared with those obtained using the commercial software COMSOL.

As shown in Fig. 13, under identical source and observation conditions and for the same physical simulation duration, both the MS-FDTD method and the FDTD method produce electric field waveforms that agree well with the COMSOL results. Notably, the MS-FDTD method exhibits a closer match with COMSOL compared to the conventional FDTD method, indicating superior accuracy and stability in modeling field propagation within complex materials. As summarized in Table II, under the relaxed CFL condition, the MS-FDTD method completes the simulation in 156.45 s, significantly outperforming the 258.46 s required by the FDTD method.

This speed advantage is attributable to the Thomas algorithm used in solving the tridiagonal systems in the MS-FDTD method. Nevertheless, due to the matrix operations involved, its per-step computational efficiency remains somewhat lower than that of standard FDTD. Regarding memory consumption, the MS-FDTD method requires approximately 30.3 MB, about twice that of the conventional FDTD method (14.7 MB), again due to the handling of tridiagonal systems. Despite a moderate increase in memory compared to the FDTD method, the MS-FDTD method still offers a manageable memory footprint—typically within several tens of megabytes—making it a practical choice for large-scale simulations requiring both high accuracy and efficient memory usage.

D. Complex Human Head Model

Fig. 14 illustrates a 3-D human brain model used to simulate electromagnetic wave propagation in highly inhomogeneous

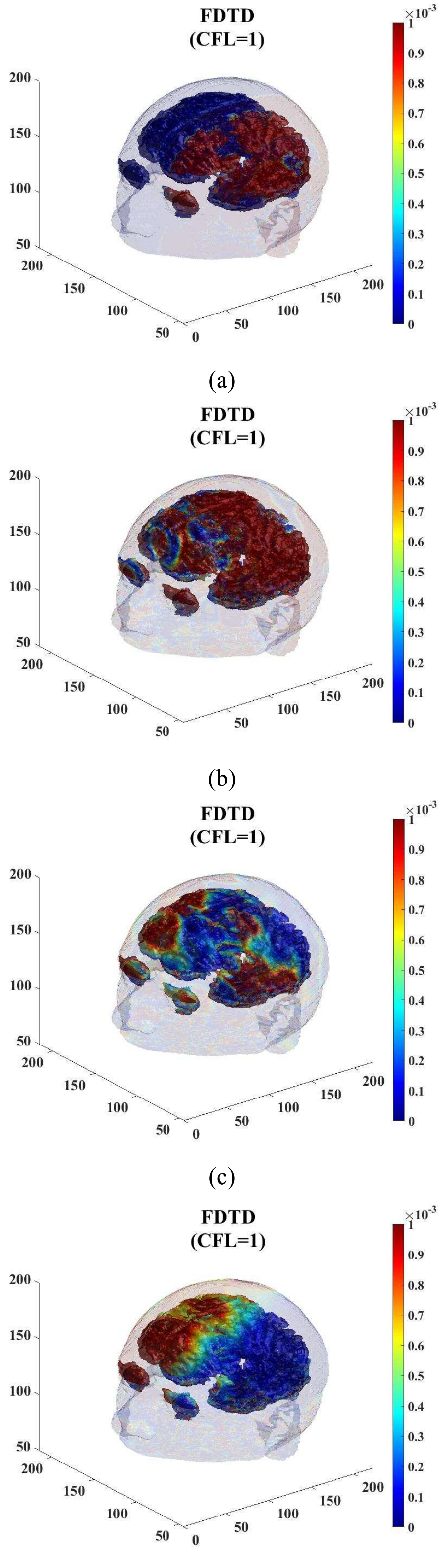

(a)

(b)

(c)

(d)

2

Fig. 15. Distributions of the squared electric field intensity ($|Ez|^2$) in the 3-D human brain model obtained by FDTD at different time steps under the CFLN = 1 condition: (a) t = 0.25 ns, (b) t = 1.25 ns, (c) t = 2.5 ns, and (d) t = 6.25 ns.

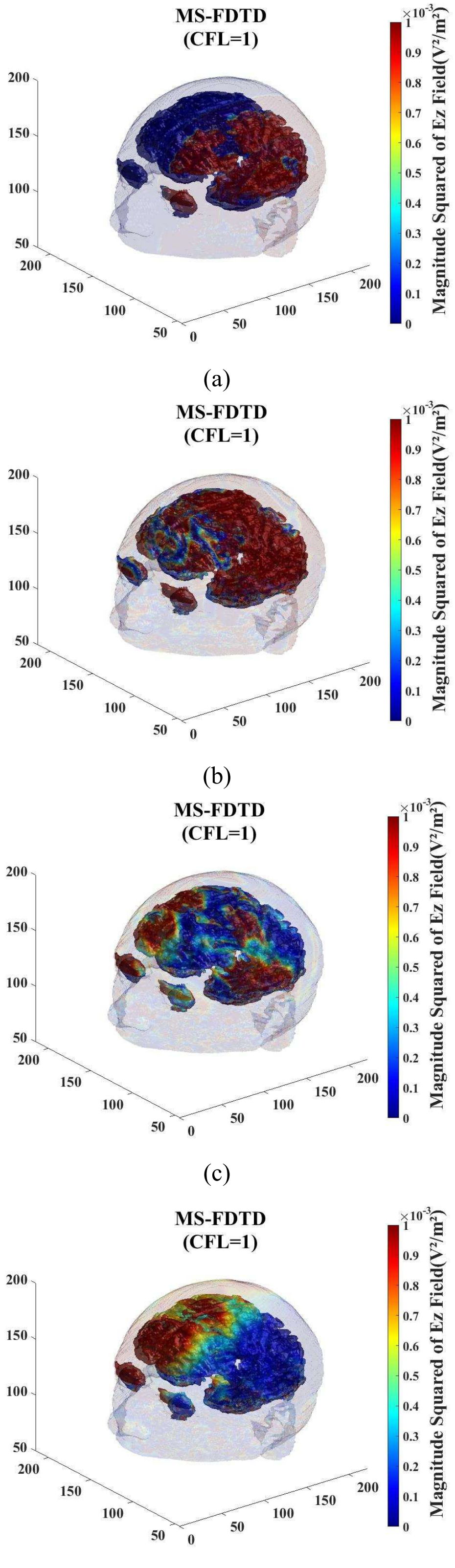

(a)

(b)

(c)

(d)

Fig. 16. Distributions of the squared electric field intensity ($|Ez|^2$) in the 3-D human brain model obtained by MS-FDTD at different time steps under the CFLN = 1 condition: (a) t = 0.25 ns, (b) t = 1.25 ns, (c) t = 2.5 ns, and (d) t = 6.25 ns.

biological tissues. The model is constructed from real medical imaging data and comprises multiple anatomical regions, each assigned a specific relative permittivity based on tissue type. This setup generates a complex electromagnetic environment

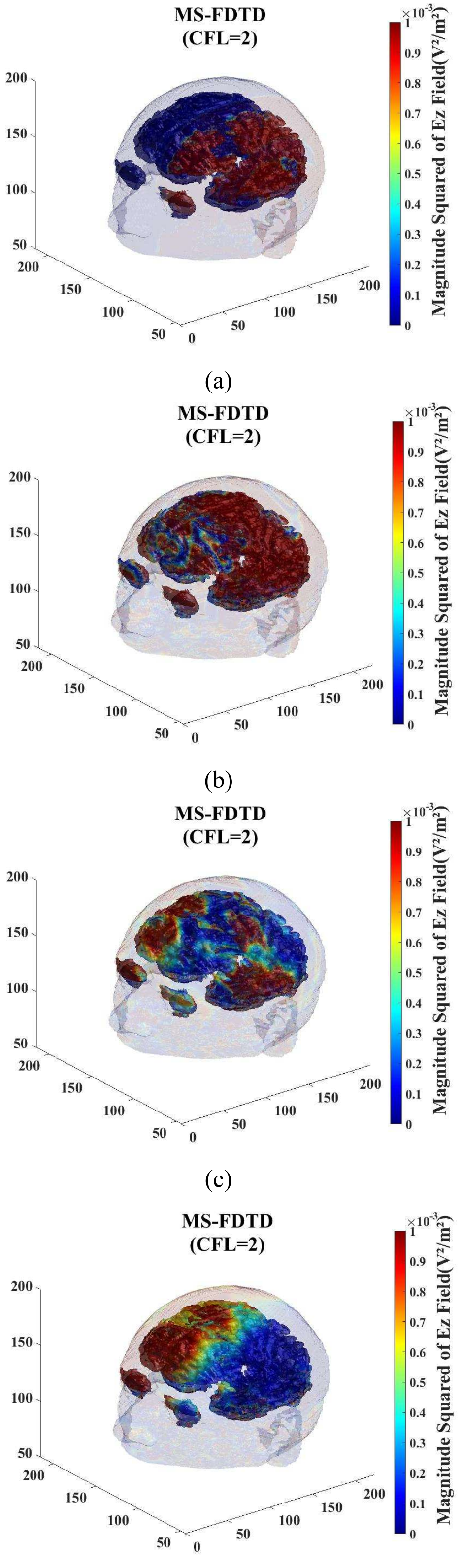

(a)

(b)

(c)

(d)

Fig. 17. Distributions of the squared electric field intensity ($|Ez|^2$) in the 3-D human brain model obtained by MS-FDTD at different time steps under the CFLN = 2 condition: (a) t = 0.25 ns, (b) t = 1.25 ns, (c) t = 2.5 ns, and (d) t = 6.25 ns.

with strong spatial heterogeneity and abrupt dielectric transitions, posing stringent requirements on numerical stability and accuracy. In this simulation, the MS-FDTD method and the FDTD method are employed with identical spatial discretization. The computational domain consists of 250 × 250 × 200 grid cells, with a ten-cell-thick UPML absorbing boundary applied along the x-direction, and PBCs imposed along the y- and z-directions. The spatial step size is uniformly set to $7.5e^{-4}$ m. To assess the method's performance under different stability conditions, two CFLN numbers are considered: CFLN = 1 ($\Delta t = 1.25e^{-12}$ s) and CFLN = 2 ($\Delta t = 2.5e^{-12}$ s). In both cases, a plane-wave source operating at approximately 26 GHz is placed outside the brain model and propagates along the x-direction. The transient electric field responses are recorded at multiple time instants within the computational domain.

Given the structural and dielectric complexity of the brain model, no analytical solution is available for this case. For this reason, a cross-comparison with the conventional FDTD method under the same CFL condition is adopted as the basic accuracy verification. The results show that MS-FDTD produces nearly identical field distributions to FDTD, thereby confirming the correctness of the proposed scheme. Figs. 15–17 present the transient electric field distributions at four distinct time instants: Fig. 15 shows the reference FDTD results at CFLN = 1, while Figs. 16 and 17 display the MS-FDTD results at CFLN = 1 and CFLN = 2, respectively. The comparisons clearly demonstrate that MS-FDTD agrees well with the conventional FDTD method under the same CFL setting, validating its accuracy. Furthermore, when the CFL number is relaxed to 2, the MS-FDTD method continues to maintain stable and accurate wave propagation in this highly inhomogeneous medium while offering improved computational efficiency.

V. CONCLUSION

In this work, a structure-preserving UPML absorbing boundary scheme is proposed within the framework of the MS-FDTD method based on the Preissmann discretization. By employing the LOD splitting strategy, the proposed UPML formulation is naturally integrated into the directionally decoupled subsystems of the MS-FDTD method, achieving both high computational efficiency and full compatibility with the existing MS structure. The method retains the geometric conservation properties of Maxwell's equations within the UPML region and enables the anisotropic damping terms to be embedded into the update process without violating structural consistency. Furthermore, the proposed approach eliminates the need for special corner or edge treatments, significantly simplifying implementation complexity. A rigorous stability analysis based on the Fourier spectral theory and eigenvalue evaluation demonstrates that the proposed scheme maintains unconditional numerical stability in 3-D settings. Extensive numerical experiments confirm that the structure-preserving UPML model exhibits excellent absorption performance and effectively suppresses reflection errors even under large CFL conditions. In addition, the results highlight the superior stability, high accuracy, and relaxed stability constraints achieved by the MS Preissmann scheme in practical electromagnetic simulations, while future work will address a systematic further investigation of CPML formulations within the MS framework.

REFERENCES

[1] K. Feng, “On difference schemes and symplectic geometry,” in *Proc. Beijing Symp. Differ. Geometry Differ. Equ., Comput. Partial Differ. Equ.*, K. Feng, Ed., Beijing, China Science Press, 1985, pp. 42–58.

[2] W. Sha, Z. Huang, X. Wu, and M. Chen, “Application of the symplectic finite-difference time-domain scheme to electromagnetic simulation,” *J. Comput. Phys.*, vol. 225, no. 1, pp. 33–50, Jul. 2007.

[3] W. Sha, X. Wu, M. Chen, and Z. Huang, “Application of the high-order symplectic FDTD scheme to the curved three-dimensional perfectly conducting objects,” *Microw. Opt. Technol. Lett.*, vol. 49, no. 4, pp. 931–934, Apr. 2007.

[4] X. Ren et al., “High-order unified symplectic FDTD scheme for the metamaterials,” *Comput. Phys. Commun.*, vol. 183, no. 6, pp. 1192–1200, Jun. 2012.

[5] W. Sha, Z. Huang, M. Chen, and X. Wu, “Survey on symplectic finite-difference time-domain schemes for Maxwell’s equations,” *IEEE Trans. Antennas Propag.*, vol. 56, no. 2, pp. 493–500, Feb. 2008.

[6] J. E. Marsden, G. W. Patrick, and S. Shkoller, “Multisymplectic geometry, variational integrators, and nonlinear PDEs,” *Commun. Math. Phys.*, vol. 199, no. 2, pp. 351–395, Dec. 1998.

[7] T. J. Bridges and S. Reich, “Multi-symplectic integrators: Numerical schemes for Hamiltonian PDEs that conserve symplecticity,” *Phys. Lett. A*, vol. 284, nos. 4–5, pp. 184–193, Jun. 2001.

[8] H. Zhu, S. Song, and Y. Chen, “Multi-symplectic wavelet collocation method for Maxwell’s equations,” *Adv. Appl. Math.*, vol. 3, no. 6, pp. 663–688, 2011.

[9] W. Cai, Y. Wang, and Y. Song, “Numerical dispersion analysis of a multi-symplectic scheme for the three dimensional Maxwell’s equations,” *J. Comput. Phys.*, vol. 234, pp. 330–352, Feb. 2013.

[10] J. Cai, Y. Wang, and Z. Qiao, “Multisymplectic Preissman scheme for the time-domain Maxwell’s equations,” *J. Math. Phys.*, vol. 50, no. 3, pp. 033510-1–033510-8, Mar. 2009.

[11] X. Yin, Y. Liu, J. Zhang, Y. Shen, and L. Yan, “Exponentially fitted multisymplectic scheme for conservative Maxwell equations with oscillary solutions,” *PLoS ONE*, vol. 16, no. 8, Aug. 2021, Art. no. e0256108.

[12] Y. Sun and P. S. P. Tse, “Symplectic and multisymplectic numerical methods for Maxwell’s equations,” *J. Comput. Phys.*, vol. 230, no. 5, pp. 2076–2094, Mar. 2011.

[13] W. Yu-Shun, W. Bin, and C. Xin, “Multisymplectic Euler box scheme for the KdV equation,” *Chin. Phys. Lett.*, vol. 24, no. 2, pp. 312–314, Feb. 2007.

[14] J. Wang, “Multisymplectic Fourier pseudospectral method for the nonlinear Schrödinger equations with wave operator,” *J. Comput. Math.*, vol. 25, no. 1, pp. 31–48, Jan. 2007.

[15] P. E. Hydon, “Multisymplectic conservation laws for differential and differential-difference equations,” *Proc. Roy. Soc. A, Math., Phys. Eng. Sci.*, vol. 461, no. 2058, pp. 1627–1637, Jun. 2005.

[16] Z. Li, M. Li, J. Wang, G. Zhu, X. Wu, and Z. Huang, “An accurate weighted parameter enhanced conformal method for dispersive FDTD method,” *IEEE Trans. Antennas Propag.*, early access, Nov. 6, 2025, doi: 10.1109/TAP.2025.3627692.

[17] P. Li, Y. Shi, L. J. Jiang, and H. Bagci, “A hybrid time-domain discontinuous Galerkin-boundary integral method for electromagnetic scattering analysis,” *IEEE Trans. Antennas Propag.*, vol. 62, no. 5, pp. 2841–2846, May 2014.

[18] Z. Chen and K. Niu., “The 3-D unconditionally stable multisymplectic FDTD method for the computational electromagnetic simulation,” *IEEE Trans. Antennas Propag.*, early access, Sep. 23, 2025, doi: 10.1109/TAP.2025.3617119.

[19] J. Shibayama, M. Muraki, J. Yamauchi, and H. Nakano, “Efficient implicit FDTD algorithm based on locally one-dimensional scheme,” *Electron. Lett.*, vol. 41, no. 19, pp. 1046–1047, Sep. 2005.

[20] E. L. Tan, “Unconditionally stable LOD–FDTD method for 3-D Maxwell’s equations,” *IEEE Microw. Wireless Compon. Lett.*, vol. 17, no. 2, pp. 85–87, Feb. 2007.

[21] D. Y. Heh and E. L. Tan, “Multiple LOD-FDTD method for inhomogeneous coupled transmission lines and stability analyses,” *IEEE Trans. Antennas Propag.*, vol. 68, no. 3, pp. 2198–2205, Mar. 2020.

[22] J.-b. Wang, B.-h. Zhou, L. Shi, and B. Chen, “Unconditionally stable FDTD method based on LOD scheme for analysis of 2-D periodic structures,” *IEEE Trans. Antennas Propag.*, vol. 60, no. 8, pp. 4003–4006, Aug. 2012.

[23] V. E. Nascimento, B.-H.-V. Borges, and F. L. Teixeira, “Split-field PML implementations for the unconditionally stable LOD-FDTD method,” *IEEE Microw. Wireless Compon. Lett.*, vol. 16, no. 7, pp. 398–400, Jul. 2006.

[24] G. Xie et al., “Extension of FLOD-FDTD method for multiterm modified Lorentz model,” *IEEE Trans. Antennas Propag.*, vol. 71, no. 11, pp. 8830–8840, Nov. 2023.

[25] L. Kong, J. Hong, and J. Zhang, “Splitting multisymplectic integrators for Maxwell’s equations,” *J. Comput. Phys.*, vol. 229, no. 11, pp. 4259–4278, Jun. 2010.

[26] G. C. X. Wang et al., “A reinforcement learning-based multiphysics optimization of comopsite material component with slot-structure in UAV system,” *IEEE Trans. Electromagn. Compat.*, early access, Nov. 13, 2015, doi: 10.1109/TEMC.2025.3627846.

[27] J. Li and P. Wu, “Unconditionally stable higher order CNAD-PML for left-handed materials,” *IEEE Trans. Antennas Propag.*, vol. 67, no. 11, pp. 7156–7161, Nov. 2019.

[28] H. L. Jiang et al., “Computationally efficient CN-PML for EM simulations,” *IEEE Trans. Microw. Theory Techn.*, vol. 67, no. 12, pp. 4646–4655, Dec. 2019.

[29] J.-F. Wang, Z. D. Chen, C. Peng, J. Li, and S. A. Ponomarenko, “Development of the recursive convolutional CFS-PML for the wave-equation-based meshless method,” *IEEE Trans. Antennas Propag.*, vol. 69, no. 6, pp. 3599–3604, Jun. 2021.

[30] J. Wang et al., “The split-field PML absorbing boundary condition for the unconditionally stable node-based LOD-RPIM method,” *IEEE Antennas Wireless Propag. Lett.*, vol. 17, pp. 1920–1924, 2018.

[31] Z.-Y. Huang, L.-H. Shi, and B. Chen, “Efficient implementation for the AH FDTD method with iterative procedure and CFS-PML,” *IEEE Trans. Antennas Propag.*, vol. 65, no. 5, pp. 2728–2733, May 2017.

[32] K. Niu et al., “Ultra-low frequency electromagnetic wave analysis in ocean-ionosphere based on ADI-FDTD combined with SIBC,” *IEEE Trans. Antennas Propag.*, Sep. 18, 2025, doi: 10.1109/TAP.2025.3608798.

[33] I. Ahmed, E. H. Khoo, and E. Li, “Development of the CPML for three-dimensional unconditionally stable LOD-FDTD method,” *IEEE Trans. Antennas Propag.*, vol. 58, no. 3, pp. 832–837, Mar. 2010.

[34] P. Y. Wu, H. L. Jiang, Y. J. Xie, and L. Q. Niu, “Three-dimensional higher order PML based on alternating direction implicit algorithm,” *IEEE Antennas Wireless Propag. Lett.*, vol. 18, pp. 2592–2596, 2019.

[35] G. Zhu et al., “A unified dispersive media and PML FDTD formulation based on the matrix exponential method,” *IEEE Trans. Microw. Theory Techn.*, vol. 72, no. 11, pp. 6336–6348, Nov. 2024.

[36] A. Ping Zhao, “Uniaxial perfectly matched layer media for an unconditionally stable 3-D ADI-FD-TD method,” *IEEE Microw. Wireless Compon. Lett.*, vol. 12, no. 12, pp. 497–499, Dec. 2002.

Zhipeng Chen was born in Anqing, Anhui, China, in 1995. He received the B.S. degree from Hefei Normal University, Hefei, China, in 2018, and the M.S. degree from Anhui University, Hefei, in 2023, where he is currently pursuing the Ph.D. degree at the School of Electronic Information Engineering.

His research interests include computational electromagnetics and finite-difference time-domain algorithms, and antennas.

Linqing Li was born in Bozhou, Anhui, China, in 1995. He received the B.S. degree from Hefei Normal University, Hefei, China, in 2018, and the M.S. degree from Anhui University, Hefei, in 2021, where he is currently pursuing the Ph.D. degree at the School of Electronic Information Engineering.

His research interests include computational electromagnetics and finite-difference time-domain algorithms, and metamaterials.

Wei E. I. Sha (Senior Member, IEEE) received the B.S. and Ph.D. degrees in electronic engineering from Anhui University, Hefei, China, in 2003 and 2008, respectively.

From July 2008 to 2017, he was a Post-Doctoral Research Fellow and later a Research Assistant Professor with the Department of Electrical and Electronic Engineering, The University of Hong Kong, Hong Kong. From March 2018 to 2019, he held a position of a Marie Skłodowska-Curie Individual Fellowship at University College London, London, U.K. In October 2017, he joined the College of Information Science and Electronic Engineering, Zhejiang University, Hangzhou, China, where he is currently a tenured Associate Professor. He has authored or co-authored over 200 peer-reviewed journal articles, 180 conference papers, 12 book chapters, and two books. His work has been cited over 11 700 times on Google Scholar, with an H-index of 58. His research focuses on theoretical and computational electromagnetics, including computational and applied electromagnetics, nonlinear and quantum electromagnetics, micro- and nano-optics, and multiphysics modeling.

Dr. Sha is a Life Member of OSA. He received multiple awards, including the PIERS Young Scientist Award in 2021, the ACES Technical Achievement Award in 2022, and the ACES-China Electromagnetics Education Ambassador Award in 2024. Nine of his students have won the best student paper awards. He has reviewed more than 60 technical journals and served on the technical program committees of over ten IEEE conferences. He is an Associate Editor of IEEE JOURNAL ON MULTISCALE AND MULTIPHYSICS COMPUTATIONAL TECHNIQUES, IEEE OPEN JOURNAL OF ANTENNAS AND PROPAGATION, IEEE ACCESS, and *Electromagnetic Science*.

Zhixiang Huang (Senior Member, IEEE) was born in Anhui, China, in 1979. He received the B.S. and Ph.D. degrees from Anhui University (AHU), Hefei, China, in 2002 and 2007, respectively.

Since 2008, he has been a Full Professor with the School of Electronic Information and Engineering, AHU. From September 2010 to 2011, he was a Visiting Scholar with Iowa State University, Ames, IA, USA. From August 2013 to October 2013, he was a Visiting Professor with The University of Hong Kong, Hong Kong. From February 2014 to 2015, he was a Visiting Professor with Beijing National Laboratory for Condensed Matter Physics, Institute of Physics, Chinese Academy of Sciences, Beijing, China. He has co-authored one monograph on the symplectic finite-difference time-domain method and two book chapters for CRC Press and InTech Publishers. He has co-authored 90 peer-reviewed journal articles included in the Web of Science Core Collection. His current research interests include time-domain numerical methods, metamaterials, and active antennas.

Dr. Huang was a recipient of the Second Prize of Science and Technology from Anhui Province Government, China, in 2015, and the National Science Foundation for Outstanding Young Scholar of China, in 2017.

Xianliang Wu was born in Bozhou, China, in 1955. He received the B.S. degree in electronic engineering from Anhui University (AHU), Hefei, China, in 1982.

He is currently a Full Professor with the Department of Electronic Engineering and the Director of the Laboratory of Electromagnetic Field and Microwave Technology, AHU, and also the Principal with Hefei Normal University, Hefei. He has authored or co-authored more than 70 articles and two books. His current research interests include electromagnetic field theory, electromagnetic scattering and inverse scattering, and wireless communication.

Prof. Wu is a Senior Member of Chinese Institute of Electronics. He was a recipient of the Ministry of Education Award for Science and Technology Progress and the Science and Technology Award, Anhui.

Kaikun Niu (Member, IEEE) was born in Anhui, China. He received the B.S. and Ph.D. degrees in electronic engineering from Anhui University (AHU), Hefei, China, in 2014 and 2019, respectively.

In 2017, he joined the Department of Electrical and Electronic Engineering, The University of Hong Kong (HKU), Hong Kong, as a Research Assistant. From 2018 to 2019, he was a Visiting Student with the King Abdullah University of Science and Technology, Thuwal, Saudi Arabia. From 2019 to 2020, he was a Post-doctoral Research Fellow with the King Abdullah University of Science and Technology. He joined the School of Electronics and Information Engineering, AHU, in 2020, where he is currently an Associate Professor. He has authored or co-authored over 50 peer-reviewed journal articles and conference papers. He holds several granted Chinese patents. His current research interests include computational electromagnetics, electromagnetic compatibility, metamaterials, and nonlinear plasmonics.

Prof. Niu received the Young Scientist Award from the 14th International Symposium on Antennas, Propagation and EM Theory (ISAPE 2024) and the Young Scientist Honorable Mention Award at the 2025 International Applied Computational Electromagnetics Society Symposium (ACES-China 2025). In addition, he advised students on research that received the Best Student Paper Awards from multiple international conferences, including the International Applied Computational Electromagnetics Society (ACES) Symposium, the IEEE International Workshop on Electromagnetics (iWEM), and the IEEE International Conference on Electronic Information and Communication Technology (ICEICT).